Modeling Techniques for Marine-Mammal Risk Assessment

Martin Siderius and Michael B. Porter

Abstract—**Propagation modeling in the ocean may be said to be a fairly mature subject, with a number of reliable and efficient acoustic models freely distributed. However, acoustic modeling to predict effects of sound on marine mammals presents some particular challenges. Standard sonar models predict the mean power levels for static receivers. However, marine-mammal researchers have shown a strong interest in being able to predict the actual time series that a moving mammal would experience as it swims through an ensonified ocean. The time series can then be used to directly model auditory models of the mammalian ear. To do this properly requires attention to subtle Doppler effects. The authors present a Gaussian-beam-tracing method that handles all these issues. Another key element needed for such models is the ability to rapidly predict three-dimensional (3-D) acoustic fields for lots of source/receiver combinations. This problem arises in trying to choose optimal locations for navy exercises, considering also a variety of hypothesized mammal-migration patterns. The authors discuss a precomputation approach to solve this problem. Finally, they examine a technique to reduce the computation needed for the one-third octave transmission loss (TL) averages. The one-third octave average is often used as a metric for the assessment of risk to mammals. The brute-force solution to this problem requires propagation modeling at many frequencies in the band. Here, the authors develop a general relationship to replace those frequency averages with much more easily computed range averages. The novelty of this approach relative to the previous range-averaging techniques is that it extends those methods to the range-dependent conditions.**

Index Terms—**Acoustics, marine mammals, sonar.**

I. Introduction

In RECENT years, evidence has accumulated indicating that human-made sound has an adverse effect on the marine environment. This has been highlighted by particular whale stranding events that have coincided with sonar activity [1]. Although sonar systems may be the most obvious form of human-made or anthropogenic underwater sound, many other sound sources exist such as shipping noise and oil exploration and drilling activities. One of the key elements to understanding the effect of sound on the marine environment is proper physics-based modeling of the sources of sound and the propagation through the ocean.

The U.S. Office of Naval Research has been addressing these issues through a program on Effects of Sound on the Marine Environment (ESME). The overall effort included a specialist on every aspect of the problem from marine-mammal population estimates and dive patterns to the anatomy and auditory modeling of marine mammals. In the course of those discussions, a wide variety of modeling needs arose, which led us to develop special modeling techniques for different applications. This paper discusses these developments.

Initially, a sort of golden solution was requested in which a marine-mammal researcher would be provided with what is sometimes called a stimulator. This is a modeling system that provides a direct prediction of the time series that a marine mammal would receive as it moved through the acoustic field, possibly taking into account the source motion (sonar on a navy ship for instance). Of course, the acoustic model should also take into account full three-dimensional effects that arise when an animal enters a complex region such as a fjord. Similarly, recently recognized focusing effects due to solitons [2] would also need to be included. Such a model might be run in a Monte Carlo fashion considering different marine-mammal dive patterns or migratory paths along with different surface ship courses. Obviously, this sort of modeling rapidly gets out of hand. A first sizable step toward this capability is to develop a Gaussian-beam-tracing algorithm for a moving mammal. A simple technique for doing this, which fully treats all the Doppler effects, is presented in Section II.

While Gaussian-beam methods provide a substantial improvement over ray methods, they often are not sufficiently accurate at low frequencies [3]. There is no universal answer as to how low a frequency is acceptable for such methods, partly because the required accuracy is in the eye of the beholder. Nevertheless, as a rough indicator, we avoid the beam-tracing approach when the water depth is less than 20 wavelengths. When small-scale ocean features such as surface ducts are important, the beam-tracing approach may break down at even higher frequencies.

The alternatives to Gaussian-beam tracing involve considerably more computationally intensive methods. Our approach to these lower frequency cases was to develop a normal-mode model for three-dimensional (3-D) environments. The approach is based on standard techniques (see [4] and references therein). However, we introduce a precalculation technique that produces a sizable reduction in the computational load. In essence, we precalculate coupling coefficients for a wedge-shaped ocean. Then, the coupling coefficient for any lat/long in the real ocean environment is obtained by identifying the corresponding depth in the wedge ocean and extracting its precalculated coupling coefficient. This approach generalizes the previous work [5] that used the adiabatic approximation (no mode coupling). The technical details of this process are described in Section III.

Manuscript received March 23, 2004; accepted June 14, 2005. This work was supported by the Office of Naval Research and was originally performed at Science Applications International Corporation. **Guest Editor: D. S. Houser.**

The authors are with the Heat, Light, and Sound Research, Inc., San Diego CA 92130 USA (e-mail: siderius@hlsresearch.com).

Digital Object Identifier 10.1109/JOE.2006.872211

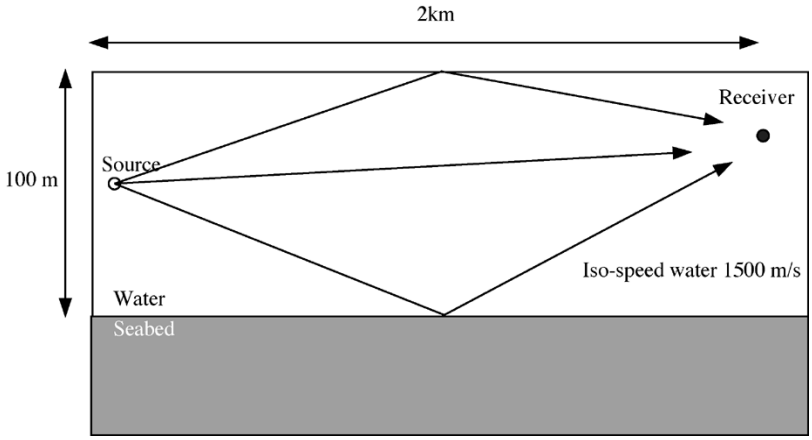

Fig. 1. Geometry for a 100-m water depth showing the source, receiver pair, and three arrivals (direct, surface reflected, and bottom reflected). The source is at 50-m depth and the receiver is at 25 m, their separation is 2 km.

The practical import is that full-wave calculations in 3-D environments can be done almost instantaneously, providing maps showing the zone of influence for the sonar or other source.

The coupled-mode approach provides an excellent complement to the beam-tracing method with a choice between the two approaches determined by frequency. As the frequency goes up, the coupled-mode option becomes computationally expensive; however, this typically occurs at a point where one feels comfortable with the accuracy of a beam-tracing approach. Finally, as an independent check, a parabolic equation model (RAM) [6] was also integrated in the modeling package.

Any model for tonal waveforms can also be used to calculate the time series using Fourier synthesis, i.e., running the model for a sequence of tones and summing the resulting pressure fields with a weighting defined by the source spectrum. The number of frequencies required in this process is roughly speaking determined by the time-bandwidth product of the band-limited channel impulse response (since that determines the number of Fourier coefficients necessary to describe that same function). Since the models are run for a sequence of tones, the run time is obviously higher than for a single tone. The Nyquist theorem tells us that we cannot get around this problem by interpolating the pressure from a coarser set of frequencies. However, oftentimes, the pressure itself can be represented as a sum of components that can be interpolated across frequency. The most obvious example is the ray/beam-tracing solution, which represents the field as a sum of echoes, each with an amplitude and delay. These quantities vary slowly with frequency (if at all) making the Gaussian-beam methods very attractive for broadband waveforms. Similarly, the normal-mode sum is based on components that can be interpolated across frequency.

In any case, even with frequency interpolation, broadband modeling is generally more computationally demanding. Meanwhile, the full time series is probably not needed in many cases to assess the impact. Instead, some coarser measure of overall noise level in a band may be a suitable metric. One measure often used is the noise in the third-octave bands [7]. In Section IV, we discuss a method for calculating energy in the third-octave bands that can be done using a single narrowband calculation.

II. Ray-Based Method for Generating Time-Series Data With a Moving Receiver

As discussed above, a "stimulator" was desired that could provide a precise model of the waveform that a moving marine mammal would hear as it moved through the ocean waveguide. Some researchers were also concerned that Doppler effects be properly included. Doppler effects have been treated in some propagation models [8]–[11]. However, these approaches do not address a broadband moving receiver in a fully range-dependent environment.

To describe the process, we begin by noting that the complex pressure field $P(\omega)$ can be represented as a sum of N arrival amplitudes $A_n(\omega)$ and delays $\tau_n(\omega)$ according to

$$P(\omega) = S(\omega) \sum_{n=1}^{N} A_n e^{i\omega\tau_n} \tag{1}$$

where $S(\omega)$ is the spectrum of the source.

The convolution theorem tells us that a product of two spectra is a convolution in the time domain. This leads to the corresponding time-domain representation for the received waveform $p(t)$, which is often written

$$p(t) = \sum_{n=1}^{N} A_n s(t - \tau_n). \tag{2}$$

where $s(t)$ is the source waveform. This representation is very intuitive, showing the sound that is heard as a sum of echoes with various amplitudes and delays.

As a concrete example, we consider the geometry shown in Fig. 1 with source at midwater depth and receiver closer to the surface. The arrival pattern is shown in Fig. 2. The top panel shows the arrival amplitudes $|A_n|$ and the lower panel shows the phase. Arrival number 14 is for the direct path between the source and the receiver and has the largest amplitude and 0° phase. Arrival 13 is from the path with a single-surface bounce and has a slightly lower amplitude than the direct (longer path) and 180° phase. As can be seen in the lower panel of Fig. 2, there are many arrivals with phase between $\pm 180°$. This reminds us

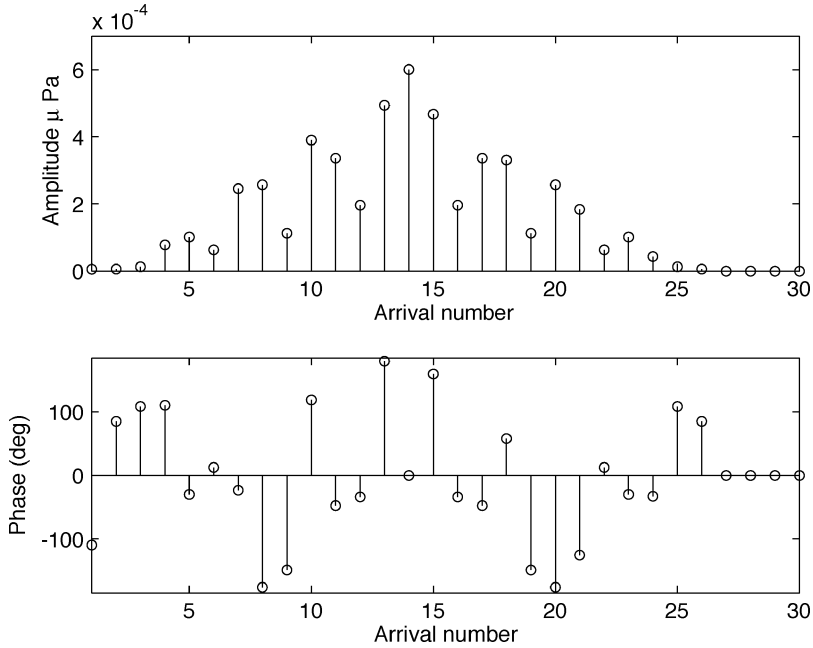

Fig. 2. Arrival amplitudes (top panel) and phase (lower panel). Note that the arrival numbers are assigned based on the launch angle starting from the surface, which leads to an arrival number for the direct path that is near the middle.

that the amplitudes A_n are really complex numbers and, therefore, (2) nonsensically delivers a complex time series from a real source waveform.

A more careful application of the convolution theorem considers the complex amplitudes and the conjugate symmetry of $P(\omega)$ that is necessary to guarantee a real received waveform. The proper result is then

$$p(t) = \sum_{n=1}^{N} \mathrm{Re}\{A_n\} s(t-\tau_n) - \mathrm{Im}\{A_n\} s^{+}(t-\tau_n) \tag{3}$$

where $s^{+} = \mathcal{H}(s)$ is the Hilbert transform of $s(t)$. The Hilbert transform is a 90° phase shift of $s(t)$ and accounts for the imaginary part of A_n. We can interpret (3) as saying that any arbitrary phase change can be understood as a weighted sum of the original waveform and its 90° phase-shifted version. The weighting controls the effective phase shift. As we have seen, the bottom reflection can yield arbitrary phase shifts. However, the paths that refract within the water column can be distorted in a similar way as the waves pass through caustics.

A. Generating Time-Series Data With Motion

The approach described in the previous section is easily modified to predict a time series for a moving receiver. One way to think about the moving-receiver problem is to imagine the stationary receivers positioned at every possible location within the environment and generating a steady-state (static) time series on each receiver. As our moving receiver proceeds through the environment, it samples, at each time step, the corresponding response from the stationary receiver's time series. In practice, we do not need to compute the entire time series for each stationary receiver but only need it for the time step that the moving receiver samples. Using (3), we use the amplitudes and delays that correspond to those at the stationary receivers at each time step. This is equivalent to the moving receiver having amplitudes and delays that change with time. For each time step, the time-dependent arrival amplitudes and delays are used in the convolution.

$$p(t) = \sum_{n=1}^{N} \mathrm{Re}\{A_n(t)\}\, s[t-\tau_n(t)] - \mathrm{Im}\{A_n(t)\}\, s^{+}(t-\tau_n(t)). \tag{4}$$

As an example, consider again the environment shown in Fig. 1. But for simplicity, assume that the source and the receiver are both at midwater depth and the receiver is moving in a range away from the source (constant depth). The position of the receiver is denoted as $r = vt$, where v is the velocity. Considering the arrivals separately, the amplitude and delay of the direct arrival, as a function of range from the source, are $A(r) = 1/r$ and $\tau = r/c$ with c as the sound speed. The received time series from a source $s(t)$ as a function of position is

$$p(t) = A(r) s\left[t - \tau(r)\right] = \frac{1}{r} s\left(t - \frac{r}{c}\right) \tag{5}$$

and substituting $r = vt$

$$p(t) = \frac{1}{vt} s\left[t\left(1 - \frac{v}{c}\right)\right]. \tag{6}$$

For a sinusoidal source function, $s(t) = \sin(\omega_0 t)$, the received time series is

$$p(t) = \frac{1}{vt} \sin\left[\omega_0 t\left(1 - \frac{v}{c}\right)\right] \tag{7}$$

which shows the familiar Doppler frequency shift of $\omega = \omega_0(1 - v/c)$. Similarly, for the surface path arriving at angle θ, $A(r) = \cos\theta/r$ and $\tau = r/c\cos\theta$ and the received time series is

$$p(t) = \left[\frac{\cos\theta}{vt}\right] s\left[t\left(1 - \frac{v}{c\cos\theta}\right)\right] \tag{8}$$

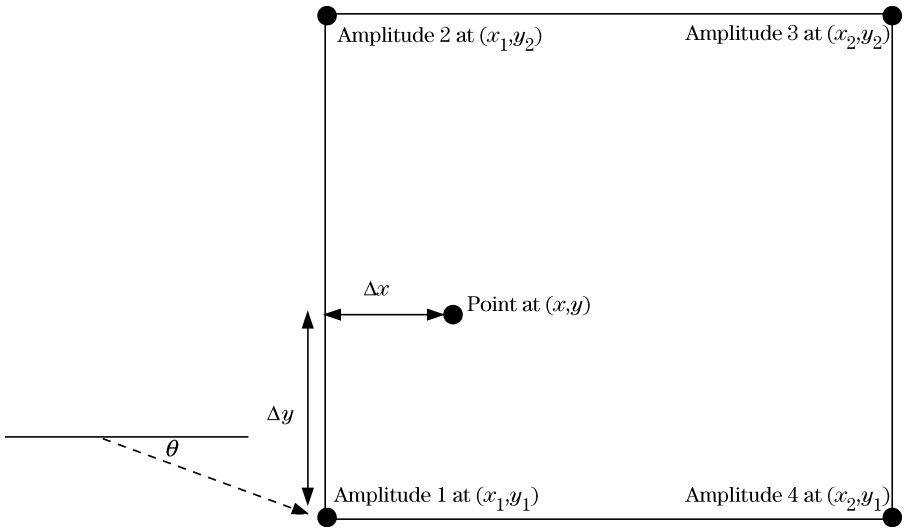

Fig. 3. Four points of the computational grid for a beam trace. The actual arrivals are computed at the four corners and any point in the interior computed through interpolation of the amplitudes and extrapolation of the delays. A sample arrival is shown traveling at angle θ.

with the Doppler-shift term and amplitude modified by the direction of the arrival. The final received time series is the sum over all arrivals.

For practical application, the arrivals' amplitudes and delays must be known at every time step and, therefore, at many positions as the receiver moves within the propagation environment. The receiver position at each time step is defined by the marine-mammal movement (or some other function for other applications), and obtaining the corresponding amplitudes and delays is the topic of the next section.

B. Ray-Arrival Interpolation and Extrapolation

Ocean acoustic models are often designed to provide an acoustic field on a regular grid. This is obviously a natural situation for displaying the acoustic field throughout the ocean waveguide. As we consider a mammal moving through the ocean, we are then forced to address the problem of interpolating the field onto the arbitrary track of the animal as it swims through the computational grid.

To fix ideas, consider four neighboring grid points, as shown in Fig. 3. To calculate the field at an interior point of the grid points, we need to identify the same arrival on the four corners and interpolate its amplitude and phase. This sounds simple enough but can be problematic since the arrivals on one grid point may not correspond to those at another. That is, the reflections and refraction effects can cause a different number of beams and different beam types on each of the grid points. For example, consider a direct arrival on one corner of the grid that is refracted away from another grid point. In this case, interpolating between these grid points for that arrival number may involve interpolation of a direct path with a bottom bounce path, and this will produce incorrect results.

To finesse this problem, we borrow an idea from finite-element methods and construct shape functions centered on each corner. The influence of these shape functions can be computed independently but their sum provides the equivalent of a bilinear interpolation. The shape functions for each corner are defined by

$$\begin{aligned} &(1-w_1) \times (1-w_2) \times A_1 \\ &(1-w_1) \times \quad w_2 \quad \times A_2 \\ &\quad w_1 \times \quad w_2 \quad \times A_3 \\ &\quad w_1 \times (1-w_2) \times A_4 \end{aligned} \tag{9}$$

where A_i represents the arrival amplitudes at each corner and the weights are

$$\begin{aligned} w_1 &= \frac{(x-x_1)}{(x_2-x_1)} \\ w_2 &= \frac{(y-y_1)}{(y_2-y_1)}. \end{aligned} \tag{10}$$

Thus, w_1 represents a proportional distance in the x direction, and w_2 represents a proportional distance in the y direction.

The four amplitudes are maintained as separate quantities, and their corresponding delays are adjusted by the ray-path travel time differences between the corners of the computational grid and (x, y). The geometry is shown in Fig. 3, with the arrival indicated as a dashed line traveling at angle θ at the lower left grid point. The delay time for that arrival is adjusted from position (x_1, y_1) to position (x, y) by the distance divided by sound speed

$$\Delta_{\text{delay}} = \frac{(\Delta x \cos\theta + \Delta y \sin\theta)}{c} \tag{11}$$

where, for example, $\Delta x = x - x_1$ is positive (increased delay) for position 1.

To summarize, the received field is constructed using (4) with an additional sum over each of the four corners (weighted amplitudes).

This technique produces a surprisingly good result even for a grid spacing of several hundred wavelengths. To illustrate, consider the same waveguide shown in Fig. 1 with a computational

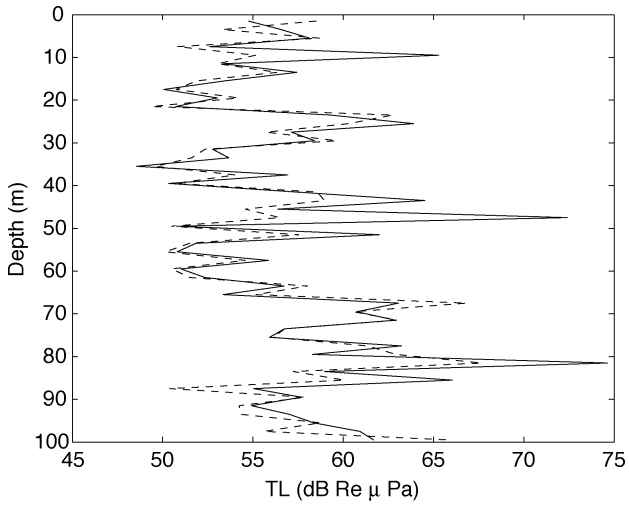

Fig. 4. TL computed at 950-m range as a function of depth. The solid line is the true field with the calculation done with grid points at depths 1.5 to 99.5 in 0.5-m increments. The dashed line is computed in between grid points using interpolation from arrivals computed at 900 and 1000 m in range and every meter in depth (on the meter).

grid of 1 m in depth and 100 m in range. We use a 3500 Hz continuous wave signal for the source and place receivers at 950 m (between range grid points) and at 1.5, 3.5, 5.5, . . ., 99.5 m (also between grid points). The results are shown in Fig. 4 where the "true" field (solid line) is computed using a very fine sampling. The result using this interpolation technique (dashed line) is in excellent agreement.

C. Frequency Dependence

In the above discussion, we have implicitly assumed that the boundary reflection coefficients are independent of frequency. As an illustration of the frequency dependence (or lack of) on beam/ray arrivals, we consider an iso-sound-speed ocean (1500 m/s) environment with 100-m water depth with geometry shown in Fig. 1. The seabed is a very fine-sand bottom (1585 m/s) (seabed sound speed, density, and attenuation for this bottom type are taken from [12]). In the top panels of Fig. 5, the bottom-reflection loss is shown for 500 and 5000 Hz along with the corresponding arrival amplitudes and delays. Note that the results for the two frequencies are identical, confirming the frequency independence of the reflection coefficient for a homogeneous halfspace.

The same quantities are plotted in the lower panels of Fig. 5, for a case where the seabed has a sound speed gradient of 10 s^{-1} in a 20-m layer. Fig. 5 shows only slight differences in both reflection loss and arrival amplitudes that occur between 500 and 5000 Hz. Even in this case, many of the arrivals have exactly the same amplitude and delay since some do not interact with the seabed. Others show slight differences that depend on the number of bottom interactions.

Obviously, more complicated layered bottoms can degrade the assumption of frequency independence. However, our experience is that this approximation is reasonable for a large variety of cases. It is worth noting in this context that detailed and accurate models of the subbottom structure are, in any case, generally not available to drive a more accurate prediction.

D. Applications of the Time-Series Simulator

As a demonstration of the method, we consider a tonal 3500-Hz source at 50-m depth and sampled at a rate of 15 000 Hz. The environment is as considered previously in Fig. 1 with the sand bottom (no gradient). We consider an idealized mammal making a perfectly horizontal transit at a depth of 25 m moving from 900 to 1000 m in range over 5 s.

The received time series in the top panel of Fig. 6 shows significant variations in the intensity as the animal moves through zones of constructive and destructive interference. This entire time series was computed in between two-range grid points separated by 100 m (or 233 wavelengths).

It is interesting to compare this variation to the steady-state field (middle panel of Fig. 6) that would be observed for a tonal plotted as a function of range. This is just a range slice of the standard transmission loss (TL) calculation for a narrowband source. The similarity of these plots indicates that the overall intensity variations can be obtained from a far simpler TL calculation. Given the agreement of these two curves (lower panel), one may conclude that the basic intensity variations can be adequately modeled from the narrowband TL plot. However, if one is interested in the finer details, such as Doppler shift, then the broadband time-series approach is effective. In Fig. 7, the spectrum of the received time series (i.e., the top panel of Fig. 6) is shown. Note how the spectrum has a clear shift of about 47 Hz for the main arrivals with some spread for the different paths.

As a second example, we consider a typical deep-water problem. The TL plot in Fig. 8 shows several common deep-water features. Wind forms a mixed layer in the upper 100 m. The combination of constant temperature with the natural increase in sound with pressure causes a slightly upward refracting layer. The result is a so-called surface duct that effectively traps energy. Surface-duct effects such as this have been implicated in the Bahamas stranding. Separately, we see a deep-cycling band of energy, which reemerges in the so-called "convergence zones" every 50–60 km in range. This deep-cycling energy corresponds to ray paths that are steep enough to escape the surface duct but are eventually turned back to the surface by the high pressure (and resulting high sound speed) at the ocean bottom.

We consider (see the expanded view in the middle panel) a hypothetical animal traveling in the mixed layer. The superimposed red line shows our dive scenario. It hears a sonar ping and dives below the mixed layer to escape the sound. As it gets below the mixed layer at 100 m, it is briefly successful in finding a quiet zone. However, as it continues deeper, it eventually enters the band of convergence-zone energy. Finally, as it continues still deeper, it again enters a quieter zone.

Our time-series simulator is capable of predicting the received waveform for the entire dive event, as shown in the lower panel of Fig. 8. The sonar transmission starts at time zero, but because of the animal's range from the source, the first arrival comes in about 30 s later. Note the quiet periods are from 12 to 13 min and from 16 min on.

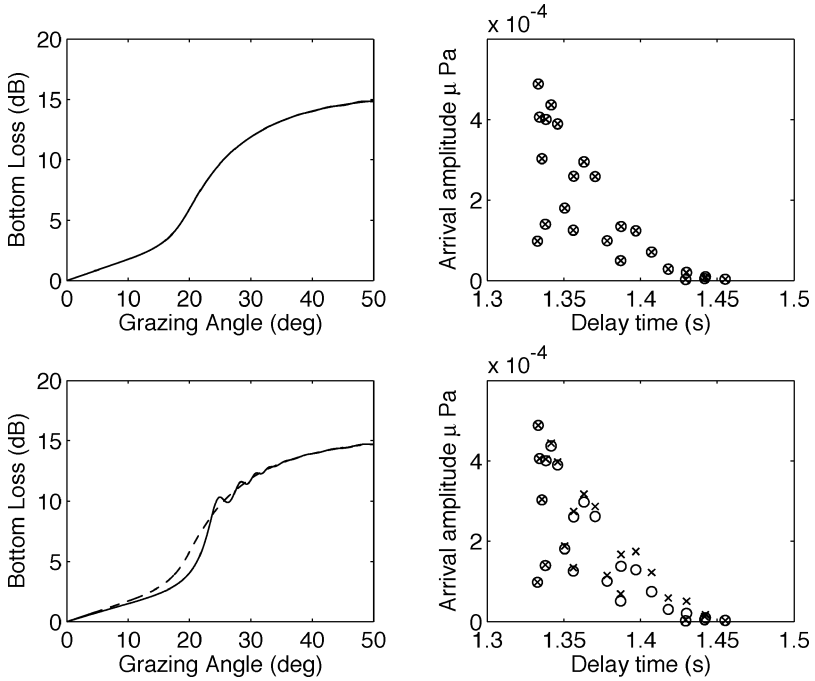

Fig. 5. Left panels show the bottom-reflection loss curves for 500 (solid) and 5000 Hz (dashed). Right panels show the arrival amplitudes and delays for 500 Hz (x) and 5000 Hz (o). The top pair of plots is for a homogeneous seabed while the bottom pair is for a sand layer with a significant gradient in sound speed. Note that the amplitudes and delays are insensitive to frequency with only slight differences for later arrivals with multiple bottom interactions in the case of the gradient bottom.

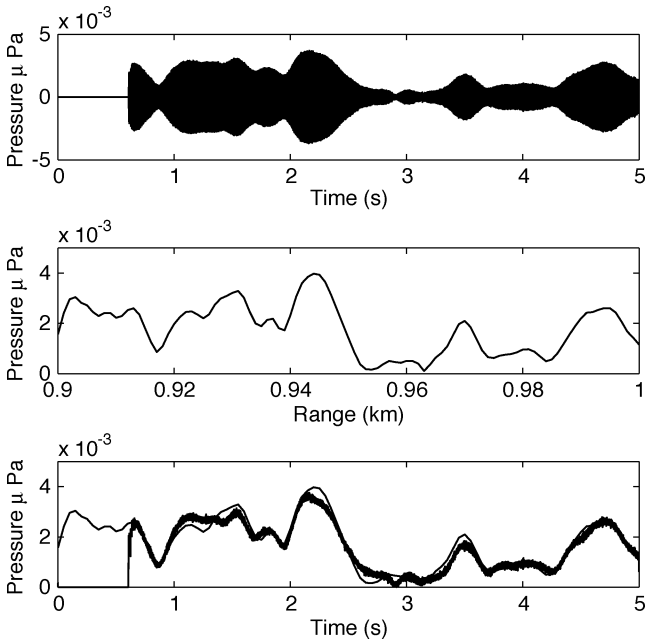

Fig. 6. Time-series simulation for a receiver moving horizontally at 20 m/s is shown in the top panel. The steady-state narrowband pressure amplitude magnitude is shown in the middle panel (as a function of range), and the lower panel compares the two (using the envelope of the received-pressure time series). The zeros at the start of the time series is due to the 0.6-s travel time.

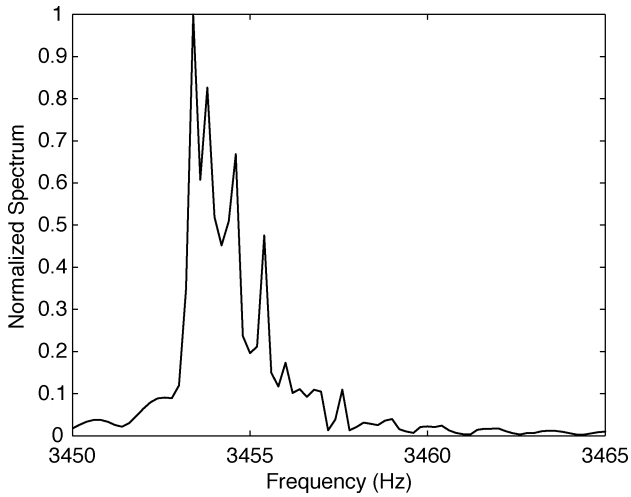

Fig. 7. Spectrum of the received waveform showing the Doppler shift and spread due to receiver motion.

III. Rapid Coupled Normal Modes

Range-dependent environments can be modeled as a series of range independent segments as indicated in Fig. 9. We begin by reviewing briefly the standard formulation. The wave equation is separated into a product of range and depth solutions with the depth equation satisfied by local normal modes Ψ_m in that segment, and the pressure field can be written as a sum over the local modes with excitation coefficients a_m (details of this formulation can be found in [4], [13])

$$P(r,z) = \sum_{m=1}^{\infty} a_m \Psi_m(r,z). \tag{12}$$

In this case, we only consider forward propagation (the one-way wave equation) and therefore only have one set of excitation coefficients in each range segment. In the first range segment containing the sound source, the excitation coefficients are proportional to the local mode function evaluated at the source depth $a_m^1 \propto \Psi_m^1(z_s)$, or in vector notation $\mathbf{a^1}$. The

pressure-field couples from one segment (j) to the adjacent segment $(j+1)$, according to a projection of mode sets between segments

$$\tilde{c}_{lm} = \int \frac{\Psi_l^{j+1}(z)\Psi_m^j(z)}{\rho_{j+1}(z)} dz. \tag{13}$$

Each $\tilde{c}_{lm}$ is an entry of the coupling matrix $\tilde{\mathbf{C}}^{\mathbf{j}}$. The phase of the mode coefficients is advanced within each range-independent segment to the border of the next segment by multiplying by the diagonal matrix $H_{mm} = \sqrt{r_{j-1}/r}\exp[ik_m(r - r_{j-1})]$. The excitation coefficients at the receiver is constructed through a cascade of coupling matrices from the first segment to the jth segment

$$\mathbf{a^j} = \mathbf{C^j H^j} \cdots \mathbf{C^3 H^3 C^2 H^2 C^1 H^1 a^1} = \mathbf{R a^1} \tag{14}$$

and the pressure field in that segment is determined using (12).

A. Precomputation of Coupling Matrices: Equivalent Wedge Ocean

The idea of rapid coupled modes is to precompute the local mode functions at all water depths between the minimum and maximum over the geographical area of interest. In this way, much of the work is already done and, for any particular source-receiver geometry, the pressure field is constructed by cascading the coupling matrices according to the bathymetry in between. The key observation is that a complicated bathymetry can be mapped to an equivalent "wedge ocean." This is shown diagrammatically in Fig. 10. The coupling matrices for each slice of the wedge ocean are precomputed. Then, to get the coupling matrix for any particular slice in the real ocean, we just extract the corresponding slice (with the same depth) from the wedge ocean. Note that in practice, we are talking about two coupling matrices for any step corresponding to upslope or downslope propagation.

The coupling matrices are of dimension $M \times M$ (for M modes) and, because the typical sampling of the mode functions is several points per wavelength, the projection matrices are of size $M \times N$, which produces a matrix usually larger (and in many cases much larger) than the coupling matrices. The mode functions themselves need only be stored at the depths for potential receivers (e.g., if the receivers only cover the top 100 m of the water column, the modes only need to be stored there).

In practice, the bathymetry usually causes the most important range dependence. The ocean and bottom sound-speed variabilities are two other obvious causes of range dependence; however, these inputs are often not readily available or accurate. When they are available, the wedge-ocean concept can be extended by calculating the coupling coefficients for the ensemble of possible depth and volume scenarios.

B. Virtual at Sea Testing (VAST)

As an example, we apply the technique to a larger area off the Virginia Capes used for VAST. The water depth (bathymetry) is shown in Fig. 11, and the sediment sound speed is shown in Fig. 12 (this type of environmental information has been combined with acoustic tools in the ESME workbench software, and details can be found in [14]). We consider 40-km radials from

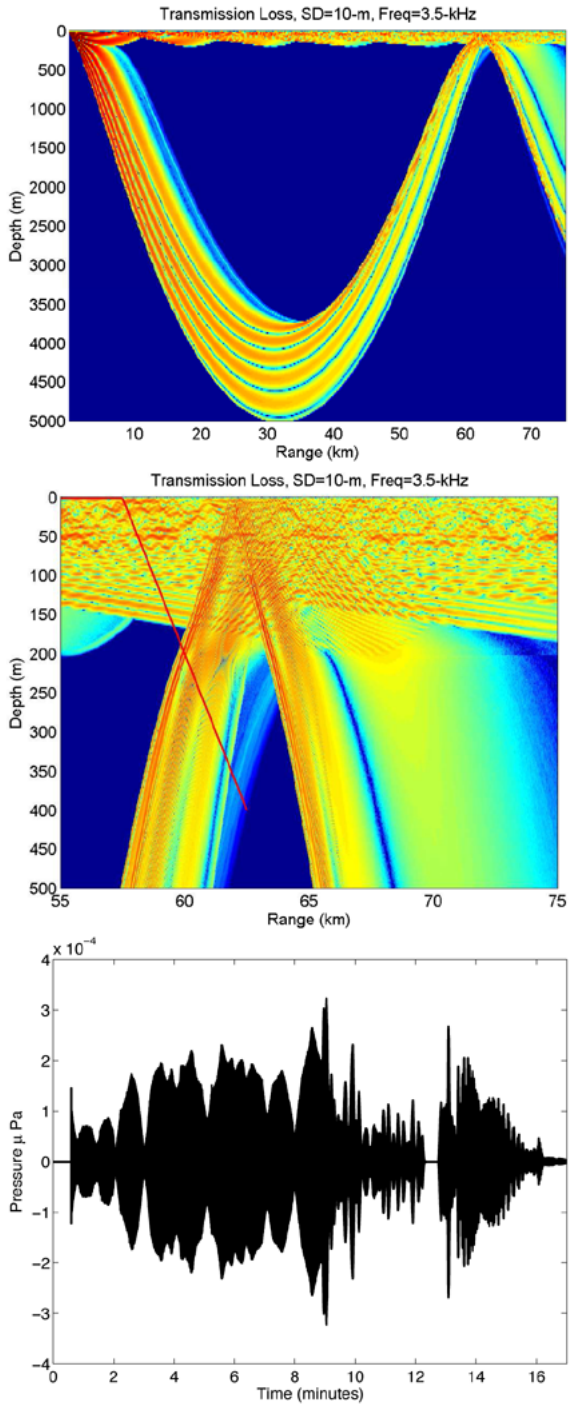

Fig. 8. Simulation for an animal diving in a deep-water environment. Top panel: TL showing surface-ducted energy and deep refracting convergence-zone paths. Middle panel: Dive path superimposed on an expanded view of the TL plot (the animal is moving near the surface for the first few kilometers and dives at about a range of 57.5 km from the source). Bottom panel: Received time series due to a 3500-Hz tonal showing quiet zones where the animal moves into acoustic shadows.

the point 36° N and 75° W. The equivalent wedge ocean for this case covers depths from 300–0 m. The central frequency of interest is 500 Hz. We first compute the TL, and this is shown along with the bathymetry in Fig. 13. In this example, the source is at 30-m depth and the slice shown is at 18 m. Near the top of the figure, some shadowing can be seen as the shallow water begins to influence the TL. Near the bottom of the figure, the

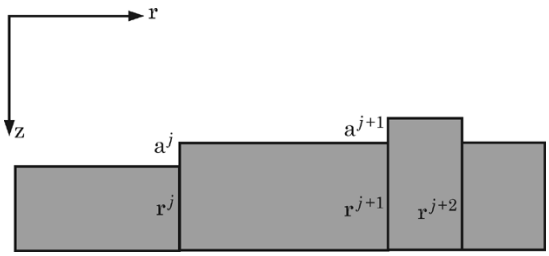

Fig. 9. Range-dependent environment is constructed as a series of range-independent segments.

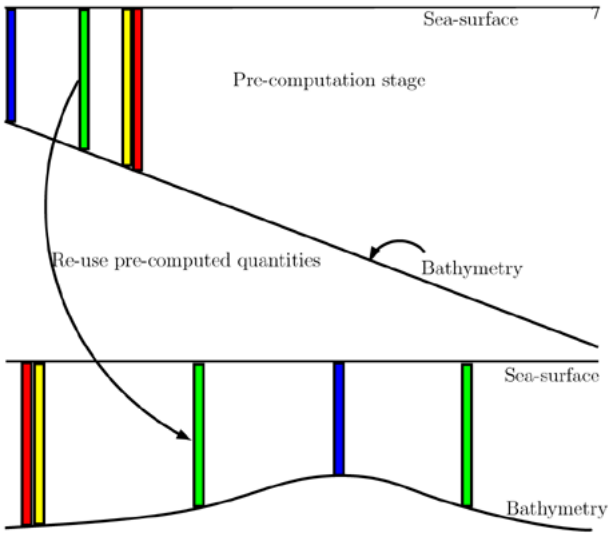

Fig. 10. Range-dependent problems for a complicated bathymetry are solved using a precomputation of all the mode functions and coupling matrices for the simple downslope and upslope problem that contains all the possible water depths. The coupling matrices and mode functions are then cascaded in the order corresponding to any desired bathymetry. This process is indicated by the colored boxes precomputed in the upper panel and reused for the lower panel.

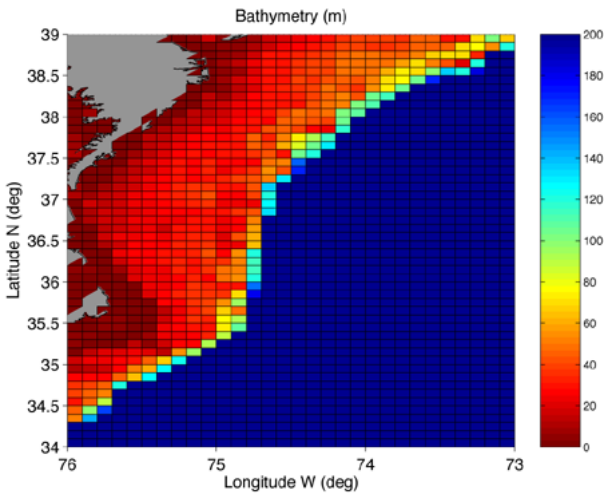

Fig. 11. Bathymetry for the Virginia Capes area (depths in meters).

shelf break begins and the water depth begins to increase and the sound tends to hug the bottom resulting in higher losses at the receiver depth.

One can imagine using the TL to create a mitigation map that translates slices like those in Fig. 13 into safe ranges to operate a sonar system. For instance, consider a source level of 230 dB

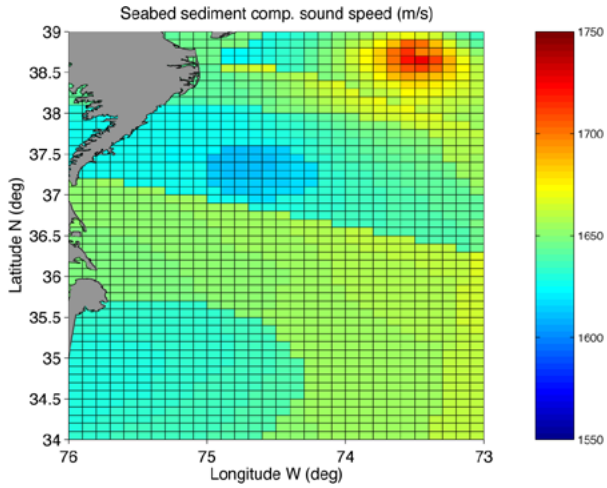

Fig. 12. Sediment sound speed (m/s) for the Virginia Capes area.

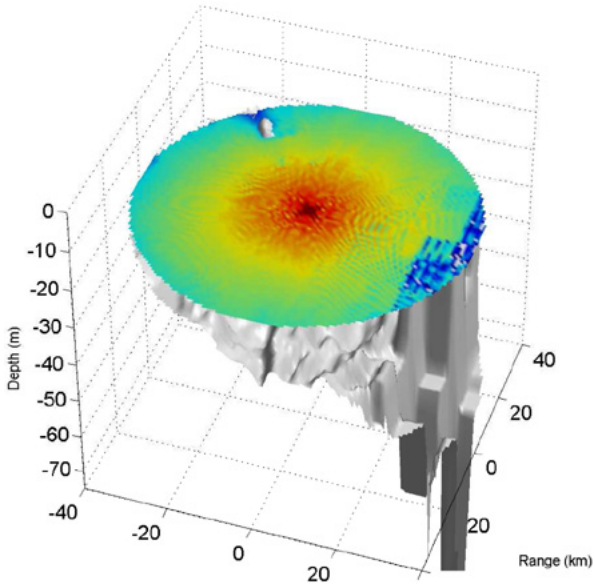

Fig. 13. TL from a source (in the middle) at 30-m depth and receiver at all bearings and 18-m depth. The color scale is in decibels re 1 μPa and ranges from 50 to 100 dB. Note the bathymetry effects on TL in the upper left and lower right portions of the slice. The gray area below shows the bathymetry.

re 1 μPa and compute the sound-intensity level as a function of range and bearing from the source position. Ranges of sonar influence can be determined and, here, we consider three zones (chosen arbitrarily): Greater than 165 dB, between 140–165 dB, and less than 140 dB. This is shown in Fig. 14 for the same source location as the TL plot of Fig. 13.

Another example for the VAST area is computing the zone (or range) of influence as a function of sonar position. In this example, the sonar is actually an explosive source and the hypothetical source positions are anywhere in the region defined in Figs. 11 and 12. In this case, peak pressure and third-octave (averaged TL) sound levels are the metrics. Fig. 15 shows the ranges of influence for a given explosion size and third-octave threshold. The effect of bathymetry is apparent from the figure as the shallow water acts as a waveguide, and the sound can propagate to longer ranges at a higher intensity. There is also an

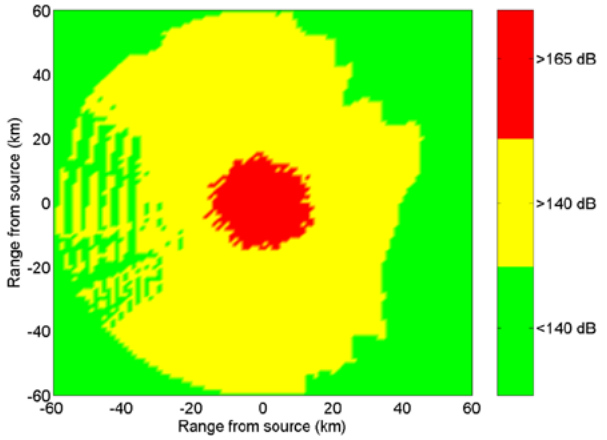

Fig. 14. Maximum sound level over the top 30 m is used to estimate a risk map for this portion of the water column relative to the range and bearing from a sonar system with a source level of 230 dB. The red, yellow, and green are threshold levels (arbitrarily chosen here) to quickly determine range of influence. Note that most of the variation in azimuth is caused by the changes in bathymetry.

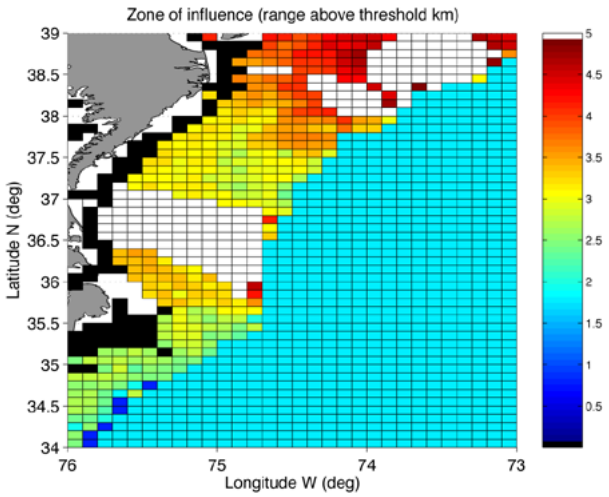

Fig. 15. Predicted zone of influence for hypothetical sound sources at various locations in the Virginia Capes area. In this case, the range of influence depends on both bathymetry and bottom properties as the more reflective seabeds allow lower loss propagation to longer ranges.

impact on propagation due to the seabed properties as the more reflective seabed types support the lower loss propagation.

The third-octave average is commonly used for determining the impact of sonar on the environment, and some useful relationships for computing these averages are given in the next section.

IV. Frequency-Averaged TL

TL plots at a single frequency inevitably show complicated interference patterns due to constructive and destructive interference of arrivals. While such complicated variation is representative of the propagation physics, the precise positions of nulls and peaks are generally difficult to predict. Further, in nature, the imperfect environment (e.g., rough surfaces and sound-speed variations) does not support the large interference effects seen in the models. More often, a general indicator of the overall sound level is needed and a standard metric used in the sonar community is the third-octave average. This is precisely defined as

$$P_{\text{ave}} = 10\log_{10}\left(\frac{1}{M}\sum_{m=1}^{M}|P(f_m)|^2\right). \tag{15}$$

Here, f_{c} is a user-selected center frequency. Upper f_{u} and lower f_{l} frequency components are related to the center frequency by $f_{\text{c}} = \sqrt{f_{\text{l}} f_{\text{u}}}$. For a one-third octave average, the upper frequency is related to the lowest by $f_{\text{u}} = 2^{1/3} f_{\text{l}}$. The center frequency can be chosen arbitrarily, but there exist some conventional center frequencies for both one-third and full octave bands.

While a third-octave average is convenient from a measurement point of view, it presents some difficulties in the modeling. In principle, the equivalent modeling process would require an expensive broadband calculation for subsequent frequency averaging. As a result, various authors (see [15] and references therein) have developed range-averaging techniques as substitutes. Range averaging can be done on a single TL calculation; however, the trick is to find formulas relating the two averages. We will show how to generalize a technique, developed by Harrison and Harrison [15], to handle range-dependent environments. We also modify their formulation to handle arbitrary windowing (e.g., the more commonly used boxcar average), as opposed to the Gaussian-weighted average.

A. Range-Independent Frequency-Range Equivalence

We begin first with the range-independent case. The results are similar to those in Harrison and Harrison; however, the derivation is different, providing a more natural lead in to the range-dependent case and allowing for choices in the way the frequency average is taken.

The frequency-domain range-independent normal-mode expression for the pressure field as a function of range r and depth z is [4]

$$P(r,z) = \frac{ie^{\frac{i\pi}{4}}}{\rho(z_s)\sqrt{8\pi}}\sum_{n=1}^{\infty}\Psi_n(z_s)\Psi_n(z)\frac{e^{ik_n r}}{\sqrt{k_n r}} \tag{16}$$

where Ψ_n are the normal mode functions, ρ is the density, and k_n the horizontal wave number. In the case of an isovelocity medium, the normal modes are $\Psi_n(z) = \sqrt{2\rho/H}\sin(n\pi z/H)$, and the wave numbers are approximated by

$$k_n = \sqrt{k_0^2 - \left(\frac{n\pi}{H}\right)^2} \approx k_o - \frac{n^2\pi^2}{2k_o H^2}. \tag{17}$$

The magnitude-squared pressure field at range R_{c} and center frequency f_{c} is

$$|P(R_{\text{c}},z,f_{\text{c}})|^2 \approx \left|\frac{1}{\rho(z_s)\sqrt{\frac{16\pi^2 f_{\text{c}} R_{\text{c}}}{c}}}\sum_{n=1}^{\infty}\Psi_n(z_s)\Psi_n(z)e^{-i\frac{n^2\pi c R_{\text{c}}}{4f_{\text{c}}H^2}}\right|^2 \tag{18}$$

where c is the speed of sound. The main change in the pressure field due to the changing frequency is from the terms in the ex-

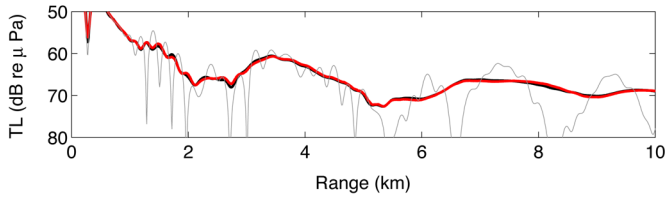

Fig. 16. Equivalence of frequency and range averaging for a range-independent environment with iso-speed water column. The source is at 50 m and the receiver at 20 m. The light gray line is the single-frequency (200 Hz) calculation, the black line is the frequency average (correct one-third octave average), and the red line is the equivalent range average. (Color version available online at http://ieeexplore.ieee.org.)

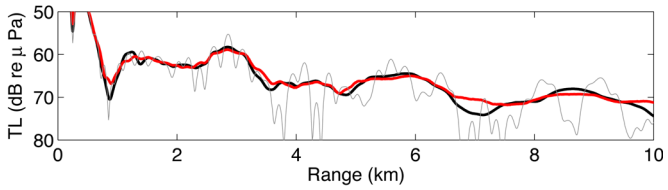

Fig. 17. Equivalence of frequency and range averaging for a range-independent environment with downward refracting (summerlike) water-column sound-speed profile. The source is at 50 m and the receiver at 20 m. The light gray line is the single-frequency (200 Hz) calculation, the black line is the frequency average (correct one-third octave average), and the red line is the equivalent range average. (Color version available online at http://ieeexplore.ieee.org.)

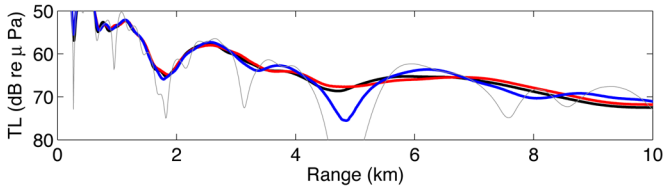

Fig. 18. Equivalence of frequency and range averaging for a range-dependent environment with iso-speed water column and bathymetry changing from 100 m at the source location to 250 m ten downrange. The source is at 50 m and the receiver at 20 m. The gray line is the single-frequency (200 Hz) calculation, the black line is the frequency average (correct one-third octave average), the red line is the equivalent range average using the relationship given by (25), and the blue line is using the range-independent formulation (20). (Color version available online at http://ieeexplore.ieee.org.)

ponent of (18). A change in frequency to f will alter the pressure field, but this can be offset by using an appropriately modified range value R. To keep $|P(R,z,f)|^2 = |P(R_c,z,f_c)|^2$, the following must be satisfied

$$\frac{n^2\pi c R}{4fH^2} = \frac{n^2\pi c R_c}{4f_c H^2} \tag{19}$$

or

$$R = \frac{f}{f_c} R_c. \tag{20}$$

Therefore, the pressure field at any frequency f in the band can be computed from the center frequency f_c using a range substitution.

An example of this equivalent range averaging can be shown for the geometry given in Fig. 1. In this example, the source is at 50-m depth and the 23rd band number is used, which has $f_l = 178$ Hz, $f_u = 224$ Hz, and $f_c = 200$ Hz. In the upper panel in Fig. 16, we show three different curves. The light-gray line is the TL calculated at the center frequency (single, 200-Hz frequency) and shows the rapid variation due to constructive and destructive interference. The solid black curve is the much more expensive third-octave calculation done through a broadband calculation. The solid red curve is the result using the range-averaging technique described above. Note that the range-average result lies on top of the true third-octave averaged result but requires no more computation than that the single frequency.

The above excellent agreement is expected since the range-averaging technique is derived based on an isovelocity medium. To show that the method is also effective for more complicated examples, we consider a summer-type profile from an experiment off San Diego having a sound speed of 1508 m/s at the surface with a thermocline that reduces the sound speed to about 1490 m/s at 40-m depth and nearly constant below that depth. The results for this downward-refracting case are shown in the lower panel of Fig. 17. Here, there are slight errors between the range-averaged and frequency-averaged results; however, in general, the agreement is excellent.

B. Frequency Averaging in Range-Dependent Environments

Considering the value of using a range averaging as opposed to frequency averaging, we next look at the generalization to more complicated range-dependent environments. The derivation is similar to the range-independent case except based on the adiabatic-mode approximation for the pressure field [4] for pressure in a range-dependent environment.

$$P(r,z) = \frac{ie^{\frac{i\pi}{4}}}{\rho(z_s)\sqrt{8\pi}} \sum_{n=1}^{\infty} \Psi_n(0,z_s)\Psi_n(r,z) \frac{e^{i\int_0^r k_n(r')dr'}}{\sqrt{\int_0^r k_n(r')dr'}} \tag{21}$$

We again assume an iso-speed water column, and want to derive the pressure fields at nearby frequencies using only the field at the center frequency f_c. That is, we define a range R such that

$$|P(R,z,f)|^2 = |P(R_c,z,f_c)|^2 \tag{22}$$

for the range-dependent case. The horizontal wave number integral is approximated by

$$\int_0^R k_n(r)dr \approx k_o R - \frac{n\pi^2}{2k_0} \int_0^R \frac{dr}{[H(r)]^2} \tag{23}$$

with $H(r)$ being the range-dependent water depth. For the range R_c at center frequency f_c to be equivalent to range R at frequency f, the following condition must be met:

$$\frac{n\pi c}{4f_c} \int_0^{R_c} \frac{dr}{[H(r)]^2} = \frac{n\pi c}{4f} \int_0^R \frac{dr}{[H(r)]^2} \tag{24}$$

This can be written as

$$\gamma(R) = \frac{f}{f_c}\gamma(R_c) \tag{25}$$

where

$$\gamma(R) = \int_0^R \frac{dr}{[H(r)]^2}. \tag{26}$$

Equation (25) has the same form as (20) but with the addition of the range integral for the range-dependent case. In essence, this formula allows us to compute the field at a new frequency by simply evaluating the field at a nearby range point. The fact that this is possible is a reflection of the existence of adiabatic invariants [16], which in turn suggests other obvious generalizations. For instance, the formulas can be extended to deep-water problems by calculating β for the given environment. We also note that some small improvements can be made by also adjusting the receiver depth at the different frequency bins to compensate for small changes in the mode function evaluated at the new receiver range (a similar approach was used for calculating the effective source–receiver geometries in [17]). This is probably not necessary for third-octave averages but may be for other applications. Finally, we note that this formula is applicable to a variety of window functions. Thus, one can use a Gaussian weighting across frequency as in [15], or one can use a flat or boxcar weighting.

As an example of the method, we modify our previous example by adding a sloping bottom with a depth of 100 m at the source location, increasing to 250 m at 10-km range. The results are shown in Fig. 18. The labeling is the same as in the previous cases except that a new solid blue curve has been added, which shows the result using the range-independent formula given by (20). Note that the corrected range-dependent range average is nearly on top of the line for the true one-third octave average, and the range-independent result is reasonable but does not follow the true average as well.

V. Conclusion

One may imagine that over the next decade, it becomes a routine to do full three-dimensional broadband modeling of sound propagation in the ocean environment. Such codes may even become fast enough to be embedded as an inner loop in still more complicated codes that do Monte Carlo simulations with varied animal populations and dive patterns, as well as varied source scenarios. However, the state of the art today does not permit such brute-force modeling so a judicious selection of approximation techniques is required.

Here, we have presented several approaches that collectively provide a powerful set of tools for modeling the effects of sound on the marine environment. The first, based on high-frequency asymptotics, uses Gaussian-beam tracing, and we have shown how the technique can be used to implement a time-series stimulator fully incorporating Doppler effects. Despite the "high frequency" approximation, such methods can be used to fairly low frequencies with perhaps 20 wavelengths in the water column. To accommodate still lower frequencies, we have discussed a coupled normal-mode approach. The two methods are very complimentary in that as one increases frequency, the normal-mode approach becomes computationally burdensome at a frequency where the beam methods are poised (i.e., sufficiently accurate) to carry the solution forward.

Finally, regardless of the fundamental acoustic model, one commonly needs to predict the simpler metric of the third-octave averaged TL. We have shown how the simple range-averaging techniques can be used to make such a broadband calculation significantly more efficient.

While these basic techniques provide a basis for studies of environmental effects of sound on the marine environment, there is clearly much more to be done. Future work will undoubtedly carry these models forward to include the refractive effects due to strong bathymetric features and/or ocean variability due to, for instance, soliton packets.

References

[1] U.S. Dept. of Commerce and Dept. of the Navy, " Bahamas Marine Mammal Stranding Event of 15–16 March 2000," Joint Interim Rep., 2001.

[2] M. Badiey, B. Katsnelson, J. Lynch, S. Pereselkov, and W. Siegmann, "Measurement and modeling of three dimensional sound intensity variations due to shallow water internal waves," *J. Acoust. Soc. Amer.*, vol. 117, no. 2, pp. 613–625, 2005.

[3] M. B. Porter and H. P. Bucker, "Gaussian beam tracing for computing ocean acoustic fields," *J. Acoust. Soc. Amer.*, vol. 82, no. 4, pp. 1349–1359, Oct. 1987.

[4] F. B. Jensen, W. A. Kuperman, M. B. Porter, and H. Schmidt, *Computational Ocean Acoustics*. New York: AIP, 1994.

[5] W. A. Kuperman, M. B. Porter, J. S. Perkins, and R. B. Evans, "Rapid computations of acoustic fields in three-dimensional ocean environments," *J. Acoust. Soc. Amer.*, vol. 89, no. 1, pp. 125–133, Jan. 1990.

[6] M. D. Collins and E. K. Westwood, "A higher-order energy conserving parabolic equation for range-dependent ocean depth, sound speed, and density," *J. Acoust. Soc. Amer.*, vol. 89, no. 3, pp. 1068–1075, 1991.

[7] DoN, "Environmental Impact Statement for the Shock Trial of the Winston S. Churchill," U.S. Dept. Navy, DDG-81, 2001.

[8] J. G. Clark, R. P. Flanagan, and N. L. Weinberg, "Multipath acoustic propagation with a moving source in a bounded deep ocean channel," *J. Acoust. Soc. Amer.*, vol. 60, no. 6, pp. 1274–1284, 1976.

[9] J. A. Neubert, "The effect of doppler on long-range sound propagation," *J. Acoust. Soc. Amer.*, vol. 62, no. 6, pp. 1404–1411, 1977.

[10] K. E. Hawker, "A normal mode theory of acoustic doppler effects in the oceanic waveguide," *J. Acoust. Soc. Amer.*, vol. 65, no. 3, pp. 675–681, Mar. 1979.

[11] H. Schmidt and W. A. Kuperman, "Spectral and modal representations of the doppler-shifted field in ocean waveguides," *J. Acoust. Soc. Amer.*, vol. 96, no. 1, pp. 386–395, Jul. 1994.

[12] "APL-UW high-Frequency Ocean Environmental Acoustic Models Handbook," Univ. Washington, Seattle, Tech. Rep. APL-UW 9407, 1994.

[13] R. B. Evans, "A coupled mode solution for acoustic propagation in a waveguide with stepwise depth variations of a penetrable bottom," *J. Acoust. Soc. Amer.*, vol. 74, no. 1, pp. 188–195, Jul. 1983.

[14] H. J. Shyu and R. Hillson, "A software workbench for estimating the effects of cumulative sound exposure in marine mammals," *IEEE J. Ocean. Eng.*, vol. 31, no. 1, pp. 8–21, Jan. 2006.

[15] C. H. Harrison and J. A. Harrison, "A simple relationship between frequency and range averages for broadband sonar," *J. Acoust. Soc. Amer.*, vol. 97, no. 2, pp. 1314–1317, 1995.

[16] W. A. Kuperman and G. L. D'Spain, *Ocean Acoustic Interference Phenomena and Signal Processing*. New York: AIP, 2001.

[17] C. Harrison and M. Siderius, "Effective parameters for matched field geoacoustic inversion in range-dependent environments," *IEEE J. Ocean. Eng.*, vol. 28, no. 3, pp. 432–445, Jul. 2003.

Martin Siderius received the B.S. degree in physics from Western Washington University, Bellingham, WA, in 1986 and the M.S. and Ph.D. degrees in electrical engineering from the University of Washington, Seattle, WA, in 1992 and 1996, respectively.

From 1990 to 1996, he was a Research Assistant at the Applied Physics Laboratory at the University of Washington. In 1996, he joined the scientific staff at the NATO Undersea Research Centre in La Spezia, Italy. Since 2001, he has been working in industry for Science Applications International Corporation and currently is at Heat, Light, and Sound Research Inc., San Diego, CA. His research interests in ocean acoustics include geoacoustic inversion, matched field processing, computational acoustics, marine mammals, acoustic communications and scattering.

Michael B. Porter received the B.S. degree in applied mathematics from the California Institute of Technology, Pasadena, in 1979 and the Ph.D. degree in engineering science and applied mathematics from Northwestern University, Evanston, IL, in 1984.

Since completing his dissertation on ocean acoustic normal modes, he has worked in underwater acoustics and acoustical oceanography in positions in the government (Naval Ocean Systems Center; Naval Research Laboratory; NATO Undersea Research Centre), in academia (New Jersey Institute of Technology and visiting positions at the University of Algarve and Scripps Institute of Oceanography), and in the private sector (Science Applications International; Heat, Light, and Sound Research). His research has included effects of oceanographic features (internal tides, surface ducts), marine mammals (dolphin sonar, mammal tracking), mine counter measures, matched-field processing, computational acoustics, underwater acoustic communications, geoacoustic inversion, and target scattering.